A New Maximum Inductive Power Transmission Capacity Tracking Method

Mohammad Hassan Ameri[*], Ali Yazdian Varjani[†], and Mustafa Mohamadian[*]

[*],[†]Department of Electrical and Computer Engineering, Tarbiat Modares University, Tehran, Iran

Abstract

In certain applications, such as IPT-based EV charger (IPTEC), any variation in alignment and distance between pickup and charger primary leads to a change in leakage and magnetic impedance magnitudes. The power transmission capacity is not always at the maximum level because of these variations. This study proposes a new low-cost tracking method that achieves the Maximum Inductive Power Transmission Capacity (MIPTC). Furthermore, in the proposed method, the exchange of information between load and source is not required. For an application such as IPTEC, the load detected by the IPTEC varies continuously with time because of the change in state of the charge. This load variation causes a significant variation in IPT resonant circuit voltage gain. However, the optimized charging output voltage should be kept constant. From the analysis of the behavior of the IPT circuit at different working frequencies and load conditions, a MIPTC operation point that is independent of load condition can be identified. Finally, the experimental results of a developed prototype IPT circuit test show the performance of the proposed method.

Key words: Electric vehicle, Inductive power transmission, Maximum transferred power point, Resonance circuit

I. INTRODUCTION

The concept of inductive power transfer (IPT) system based on the elimination of physical contact between the source and the consumer of electrical energy was introduced approximately 100 years ago [1], [2]. The low transfer power rating along with the EMI is the main barrier in employing this technique [3], [4]. Recent developments in semiconductor technology allows switching frequency to be increased, resulting in higher power transfer rating [5].

A circuit can operate at high frequency naturally using resonant converter by adding capacitors in series or parallel in one or both sides of an IPT [1], [2], [6]–[9]. Four kinds of resonance converters, namely, series–series, parallel–series, series–parallel, and parallel–parallel resonant converters, exist based on resonant capacitors that are added to the primary and/or secondary IPT converter. A resonance converter is utilized in charger application to reduce switching loss and improve power factor [10]-[12]. Herein,

different kinds of resonance topologies have been presented for electric vehicle (EV) charger; however, LLC and LCL are more widely used [12], [13].

Various IPT-based applications have been utilized in cellphone chargers, robotics, magnetic levitation trains, and EV chargers [8]-[11]. IPT-based EV chargers (IPTECs) offer further development of conventional EV chargers. One of the best proposed structures for the IPTEC is the "disc-type transformer," which can be placed under the vehicle [19]. In [20], [21], [22], the geometries of a pair of spiral coils are optimized to maximize the inductive power transmission. In [5], a control method for frequency optimization based on switching loss is proposed. This method uses a reversed resonance capacitor to improve efficiency. The maximum power transfer capacity can be achieved by the appropriate IPT switching frequency considering the magnetic parameters of an IPT transformer [9]. The switching frequency of IPTECs is normally constant [6]. However, the magnetic parameters and frequency of Maximum Inductive Power Transmission Capacity (MIPTC) should be adapted because of the different positions of the secondary disc-type transformer in the inductive EV charger relative to the primary.

In [23], a monitoring system with a closed loop for

fine-tuning the resonance frequency of the secondary coil circuit is presented. In this method, prior to starting battery charging (power transmission), the system scans the frequency around the given resonance frequency on the primary coil and measures the output voltage on the secondary coil until a desirable voltage level is achieved. In [23], the IPT system uses parallel–parallel resonance converter, which causes a large variation in secondary voltage for different load sizes. This method also needs a wireless connection in the secondary side of IPT, thus increasing the cost and decreasing reliability.

The coupling and the consequent power transfer vary as a function of distance between primary and secondary coils along the transmission axis and orientation [24]. An adaptive frequency tuning technique by using secondary voltage feedback is demonstrated in [24], compensating for efficiency variations encountered in a secondary fixed-load when the primary-to-secondary distance and/or orientation are varied. The most important problem of this method is the necessity of fixing load and transferring data from secondary to primary.

In EV charging, the vehicle should be placed exactly at a specified location. Any position mismatch or any variation in vehicle height causes a reduction in charger transfer power capacity. However, a general EV charger should be able to transfer the power demand of an EV independent of vehicle size and height. In addition, the charger should be user-friendly and inexpensive.

This study proposes a new tracking method to determine the MIPTC frequency for different load circumstances. This method does not need any kind of information regarding load specifications and conditions, such as load current (state of the charge), relative position of the primary (charger), and pickup (EV). For formulating the proposed method, all equations of the IPT-based series–series and parallel–parallel resonance converters are rewritten to show a MIPTC operation point that is independent of load magnitude.

This section is followed by an introduction to the IPT system principles, a different analysis of IPT resonance converters, and the proposed circuit topology for EV inductive charger in Section II. In Section III, a new algorithm for tracking the frequency of MIPTC is proposed. In Section IV, the experimental results are shown to validate the performance of the proposed method.

II. INDUCTIVE POWER TRANSFER SYSTEM

In principle, the IPT is a power transformer with a large air gap; the primary is connected to the source, and the secondary is connected to the load. Fig. 1 illustrates the IPT concept block diagram that usually consists of an AC/DC cascaded in a high-frequency DC/AC converter in the primary side, a transformer, and an AC/DC converter in the secondary side.
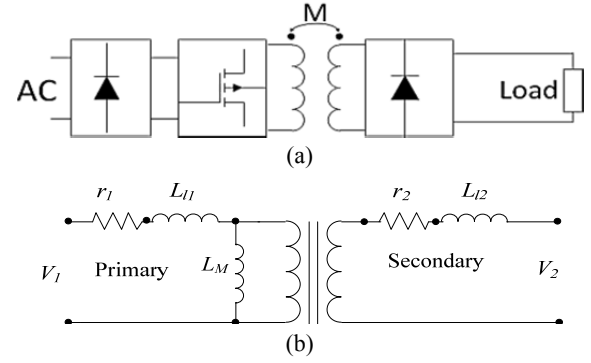

Fig. 1. Inductive power transformer: (a) IPT block diagram and (b) equivalent circuit of the transformer.
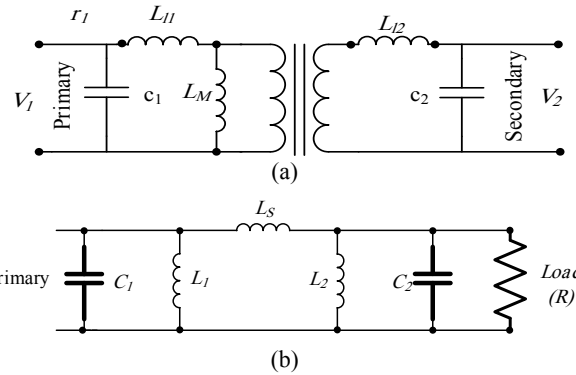

Fig. 2. Parallel–parallel resonante circuit: (a). T model and (b) π model of PPR–IPT.

The large air gap of an IPT transformer increases the flux leakage and consequently results in higher leakage inductances compared with conventional transformers. The efficiency and power transmission capacity of IPT is normally less than 50% [25].

IPT with resonance capacitors can be modeled as a series–series (SSR), series–parallel (SPR), parallel–parallel (PPR), or parallel–series resonant (PSR) converters. Although a large number of mathematical models for IPT-based resonance converters have been proposed in the literature, no analysis to determine the entire extremum point of the resonance converter gain has been conducted. In the subsequent sections, the analyses of the power–frequency variation of PPR and SSR converters are presented.

A. Parallel–Parallel Resonance Converters

As illustrated in Fig. 2(a), in a parallel–parallel resonant IPT converter (PPR–IPT), the capacitors are in parallel at the input and output of the circuit. As shown in Fig. 2(b), for simplifying equations, the transformer is modeled as π in which:

$$L_s = L_{l1} + L_{l2} + \frac{L_{l1}L_{l2}}{L_M},$$

$$L_1 = L_M + L_{l2} + \frac{L_M L_{l2}}{L_{l1}}, \quad . \tag{1}$$
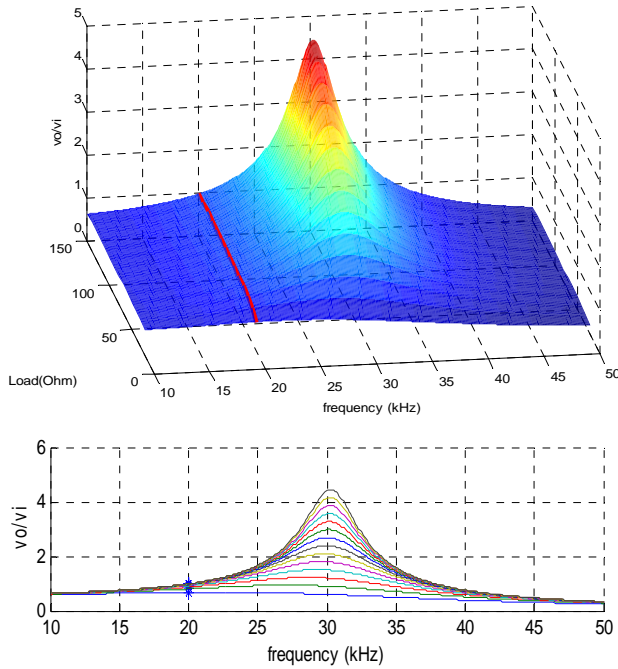
$$L_2 = L_M + L_{l1} + \frac{L_M L_{l1}}{L_{l2}}$$

Fig. 3. Variation of $|V_o/V_i|$.

Assuming resistive load, the load power is related to load voltage. Therefore, the (V_o/V_i) transfer function is calculated using Eqs. (2) and (3):

$$h(s) = \frac{V_o(s)}{V_i(s)} = \frac{R \parallel \frac{1}{C_2 s} \parallel L_2 s}{R \parallel \frac{1}{C_2 s} \parallel L_2 s + L_s s}, \tag{2}$$

$$h(s) = \frac{V_o(s)}{V_i(s)} = \frac{R L_2}{R(L_2 + L_s) + L_2 L_s s + R L_2 L_s C_2 s^2}. \tag{3}$$

The magnitude of the impulse function $H(w)$ is given in Eq. (4), which for simplification can be rewritten in terms of resonance frequency ($\omega = \frac{1}{\sqrt{C_2 L_2}}$) as Eq. (5):

$$H(\omega) = \left| \frac{V_o}{V_i}(\omega) \right| = \frac{R L_2}{\sqrt{(R(L_2 + L_s) - R L_2 L_s C_2 \omega^2)^2 + (L_2 L_s \omega)^2}}, \tag{4}$$

$$\left| \frac{V_o}{V_i}(\omega_r) \right| = \frac{R L_2}{\sqrt{R^2 L_2^2 + \frac{L_s^2 L_2^2}{C_2}}} = \frac{R}{\sqrt{R^2 + \frac{L_s^2}{C_2 L_2}}} < 1. \tag{5}$$

As shown in Eq. (5), at the resonance frequency, the voltage gain (V_o/V_i) is related to the load (R) and the transformer parameters, and its gain is less than 1 for all loads. Fig. 3 depicts the variation of (V_o/V_i) as a function of the frequency and the load. The red line represents the voltage ratio at the resonance frequency for different loads. As expected, the voltage ratio presents a different value for different values of load.

The peak coordinates of the $|V_o/V_i|$ curve is MIPTC. The MIPTC can be determined by setting the derivative of Eq. (4) equal to zero, as expressed in Eq. (6). The maximum value of $|V_o/V_i|$ is given in Eq. (7). Notably, Eq. (6) presents a unique solution if the expression under the radical is greater than or equal to zero. Accordingly, the acceptable range of the load (R)
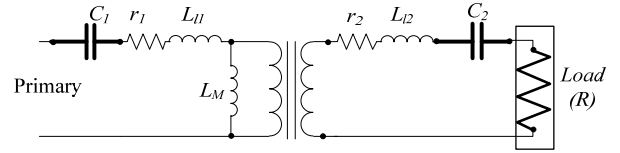

Fig. 4. Series–series resonant IPT.

is shown in Eq. (8). For other values of R, Eq. (4) will show no maximum value. Eq. (8) also shows that, in PPR–IPT, the maximum value of V_o is proportional to the size of R.

$$\frac{d\left|\frac{V_o}{V_i}\right|}{d\omega} = 0 \Rightarrow \omega_c = \sqrt{\frac{(L_2 + L_s)}{C_2 L_s L_2} - \frac{1}{2R^2 C_2^2}} \tag{6}$$

$$\left(\frac{V_o}{V_i}\right)_{max} = \frac{\sqrt{2} R^2 C_2}{L_s} \frac{1}{\sqrt{\frac{2R^2 C_2}{L_s} + \frac{2R^2 C_2}{L_2} - 1}} \tag{7}$$

$$R \geq \sqrt{\frac{L_s L_2}{2C_2(L_s + L_2)}} \tag{8}$$

B. Series–Series Resonant IPT

In the series–series resonant IPT converter (SSR–IPT), the capacitors are in series at the primary and secondary of IPT, as shown in Fig. 4. The major goal of this configuration is eliminating leakage (series) inductance [10]. The equations of V_o/V_i of SSR–IPT are given in Eqs. (9)–(11). Assuming $L_{l2} = L_{l1} = L$ and $C_1 = C_2 = C$, Eq. (11) can be rewritten as Eq. (12):

$$\frac{V_o}{V_i} = \frac{(R + \frac{1}{C_2 s} + L_{l2} s) \parallel L_M}{(R + \frac{1}{C_2 s} + L_{l2} s) \parallel L_M + \frac{1}{C_1 s} + L_{l1} s} \tag{9}$$

$$h(s) = \frac{V_o(s)}{V_i(s)} =$$

$$\left(\frac{L_M L L_{l2} C_2 s^3 + L_M R C_2 s^2 + L_M s}{L_M L L_{l2} C_2 s^3 + L_M R C_2 s^2 + L_M s + \frac{(L_{l1} C_1 s^2 + 1)}{C_1 s}(C_2(L_M + L_2) s^2 + R C_2 s + 1)} \right) \times$$

$$\left(\frac{R C_2 s}{L_{l2} C_2 s^2 + R C_2 s + 1} \right) \tag{10}$$

$$h(s) = \frac{V_o(s)}{V_i(s)} = \frac{L_M C^2 R s^3}{C^2 L(L + 2L_M) s^4 + C^2 R(L + L_M) s^3 + 2C(L_M + L) s^2 + RCs + 1} \tag{11}$$

$$\left| \frac{V_o}{V_i} \right| = \sqrt{\frac{(L_M C^2 R \omega^3)^2}{\left[C^2 L(L + 2L_M)\omega^4 - 2C(L_M + L)\omega^2 + 1\right]^2 + \left[C^2 R(L + L_M)\omega^3 - RC\omega\right]^2}}$$

$$\begin{cases} \left(\frac{V_o}{V_i}\right)_{\omega = \omega_R} = 1 \\ \omega_R = \frac{1}{\sqrt{L_{l1} C_1}} = \frac{1}{\sqrt{L_{l2} C_2}} \end{cases} \tag{12}$$

As shown in Eq. (12), the gain of the input–output impulse function in the resonance frequency ($\omega = \frac{1}{\sqrt{C_2 L_{l2}}} = \frac{1}{\sqrt{C_1 L_{l1}}} = \frac{1}{\sqrt{CL}}$) is equal to 1. In other words, the transferred power capacity at the resonance frequency is independent of R [17].

Previous works have shown that the efficiency at this point is the maximum, but finding a point with maximum power transfer capacity is a new concept.

Fig. 5(a) shows the V_o/V_i curve as a function of load and frequency. As shown in Fig. 5(a), the curve has two extrema or two MIPTC points: the first extremum (F_1), which is the global extremum and its value, is dependent on the load value; the second extremum (F_2), which occurs at a designed resonant frequency ($\omega = \frac{1}{\sqrt{CL}}$) and its value, is independent of load variation and bears a value of 1 for all loads. If R approaches infinity (no load), then Eq. (12) can be rewritten as Eq. (13), which shows that V_o/V_i presents an extremum at $\omega = \frac{1}{\sqrt{C(L_M+L)}}$ and that its value approaches infinity, and any extremum does not occur at ($\omega = \frac{1}{\sqrt{CL}}$), as illustrated in Fig. 5(a).

$$\left|\frac{V_o}{V_i}\right| = \left|\frac{L_M C \omega^2}{C(L+L_M)\omega^2 - 1}\right| \quad (13)$$

Fig. 5(b) shows the V_o/V_i curve as a function of the magnetic inductance and frequency. The frequency and amplitude of the first extremum of the V_o/V_i curve varies by changing magnetic inductance. In addition, Fig. 7(b) shows that the second extremum does not occur for small magnetic inductance ($L_M < 0.2$ mH). Notably, a small inductance means a large air gap or a small coefficient factor (K). By assuming $L_M \ll L$, Eq. (13) can be rewritten as Eq. (14). This equation shows that, by eliminating L_M, V_o/V_i shows no extremum point. Instead, the curve shows an asymptotic expansion at a designed resonance frequency. Eq. (16) shows that the V_o/V_i curve presents only one peak for small L_M that occurs close to $\omega = \frac{1}{\sqrt{CL}}$.

$$\left|\frac{V_o}{V_i}\right| = \sqrt{\frac{(L_M C^2 R \omega^3)^2}{(CL\omega^2-1)^2(RC\omega+1)}} = \frac{(L_M C^2 R \omega^3)}{|CL\omega^2-1|}\frac{1}{\sqrt{(RC\omega+1)}} \quad (14)$$

The comparison of Figs. 3 and 5a shows that, in the PPR converter, the peak of the V_o/V_i curve does not occur at the resonance frequency. In other words, the maximum value of $|V_o/V_i|$ does not accrue at $\omega = \frac{1}{\sqrt{C_2 L_2}}$.

For applications such as battery chargers, the load varies continuously. If the voltage gain of the operation point is sensitive to the load value, then the load voltage is varied during the charging process. The comparison of the analytical analysis of SSR–IPT and PPR–IPT converters shows that SSR is the best topology for EV chargers. Therefore, this study aims to track the frequency of the MIPTC in the IPT power–frequency curve that does not change during load variation.

III. TRACKING THE FREQUENCY OF MIPTC

The different air gap permeabilities and resonance capacitor tolerance capacities in the initial IPT frequency are not always at the optimum working frequency because of the variations in conditions, such as changing the position of the primary and secondary with respect to each other. For example, several
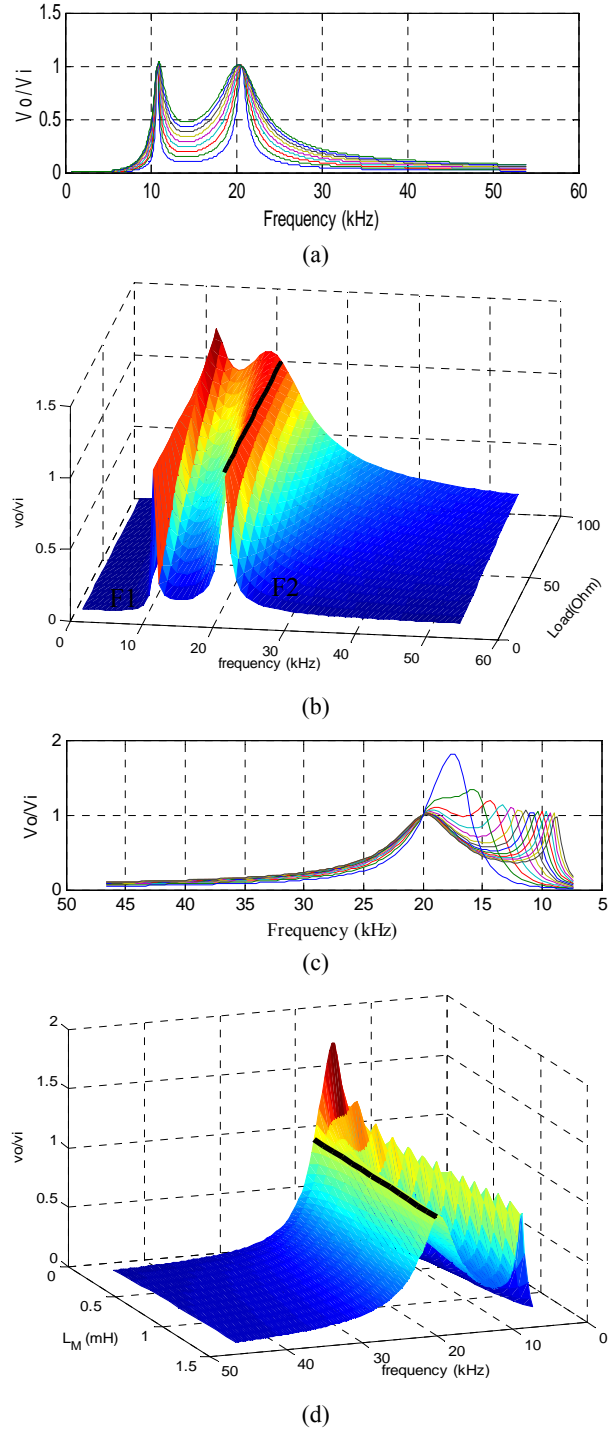

Fig. 5. (a) Load–frequency variation curve of $|V_o/V_i|$; (b) 3D view; (c) L_M–frequency variation of $|V_o/V_i|$; and (d) 3D view.

IPTECs use coreless transformers, as shown in Fig. 10, where the primary winding is fixed on the ground and the secondary is installed on the car and may be positioned above the primary winding in any direction or alignment [14], [19], [26]–[28]. The value of MIPTC frequency is dependent on the resonance topology, capacitor capacity, and magnetic parameters of the IPT. Assuming constant capacitance, MIPTC frequency is a
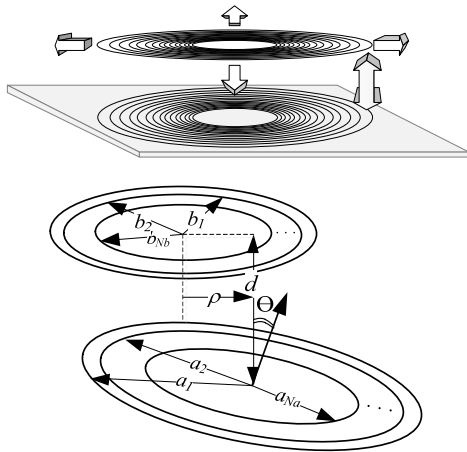
Fig. 6. Coreless transformer with spiral winding.

TABLE I
SSR–IPT PARAMETERS

Primary and secondary leakage inductances (L_{l1}, L_{l2})	701 µH
Magnetic inductance (L_M)	780 µH
Primary and secondary series resonance capacitors	100 nF
Load	60 Ω
Input voltage	100 V

function of magnetic parameters, such as self and mutual inductance. Self and mutual inductance of the coreless transformer (Fig. 6) are functions of the number of windings, inner and outer diameters of each side, distance between primary and secondary (d), and distance between the axes (ρ) [29]. Therefore, assuming fixed capacitor sizes, the resonance frequency of IPT is sensitive to the relative position of the EV and charger. Thus, at the beginning of any power transfer process, the MIPTC frequency should be calculated for any new secondary (pickup) position, as mentioned previously.

Considering the complexity of IPT inductance formulas and the high calculation burden, the inductances are difficult to calculate with MIPTC frequency for every usage. Therefore, the value of MIPTC frequency should be estimated. The third winding method is used as one of the presented estimation techniques [3]. This method suffers from the physical limitations of third winding placement in the EV charger applications and low accuracy caused by uncertain received flux from the primary process. As expressed in the "Introduction" section of this paper, the maximum transfer power capacity can be achieved using the load voltage feedback [17]. The major problem of this method is the necessity of transferring information from the secondary side to the primary side. This information feedback reduces the system reliability and increases its complexity and cost. In addition, this method works only at fixed load conditions [17]. Therefore, a tracking method, which determines the MIPTC by using a primary measurable variable, is proposed as the optimum

problem-solving approach.

Fig. 7(a) illustrates the output voltage versus frequency for the SSR–IPT with parameters shown in Table I. At a certain working frequency, the output voltage reached its maximum value. At this point, the MIPTC working frequency is equal to the series LC resonance frequency in SSRC. The switching pattern of the primary converter is the square wave mode with 50% duty ratio. Fig. 7(b) shows the input and output active power curves versus frequency. The frequency variation of the input reactive power is also shown in Fig. 7(c). The input and output active powers reached its maximum, and the reactive power is zero at MIPTC. As explained in Section II, the efficiency of IPT (illustrated in Fig. 7(d) can be regarded as approximately constant around the MIPTC working frequency. Therefore, feedback from the secondary variable can be replaced by feedback from the primary variable.

Power calculations are the most important factors in the detection of the maximum power frequency tracking process.

Losses of every power electronic converter include conduction (P_{cond}) and switching loss (P_{SW}). Switching losses consist of switch turn-on and turn-off losses. Equation (15) shows an inverter loss, in which C_{oss}, f_{sw}, I_{load}, I_{gate}, and R_{on} correspondingly denote the power MOSFET output capacitance, switching frequency, load current, gate current, and switch-on resistance. Given that the two switches are always turned on all the time, the $P_{each-SW}$ is multiplied by 2.

$$P_{converter} = 2\left(\underbrace{\underbrace{\left(C_{oss} \times V_{in}^2 \times f_{SW} \times I_{Load}\right)\Big/ I_{Gate}}_{P_{sw}} + \underbrace{R_{on}I_{Load}^2}_{P_{cond}}}_{P_{each-SW}}\right) \quad (15)$$

Fig. 7(e) demonstrates the simulation results of switching loss for the expressed model. A similar behavior is observed in the diagram of changes in the input (Pin-conv) and output power (Pout-conv) of the primary converter. Fig. 7(e) shows that the peaks of the two diagrams present the same frequency and similar amplitudes. For further explanation, the "loss curve" of the primary side converter is shown in Fig. 8. Fig. 8 indicates that the conduction losses of the converter represent a function of load current. By contrast, switching loss is only a linear function of changes in frequency. Investigation of the diagrams of input power and switching loss of the primary side inverter confirms that the average of DC bus power can be used instead of its output power to analyze the process of power transmission in inductive power transfer systems. Given the current and DC voltage, the reading of the input power does not need any complicated calculation and is calculable only by a multiplication operation. The reduction of power calculation operations enhances the speed of running the optimization algorithm. In all the tests shown in Fig. 10, the tracking time is less than 100 ms.

A perturb and observe method [30] can be used as the proposed MIPTC tracker algorithm. This method demonstrates that the process is repeated until the MIPTC is reached.
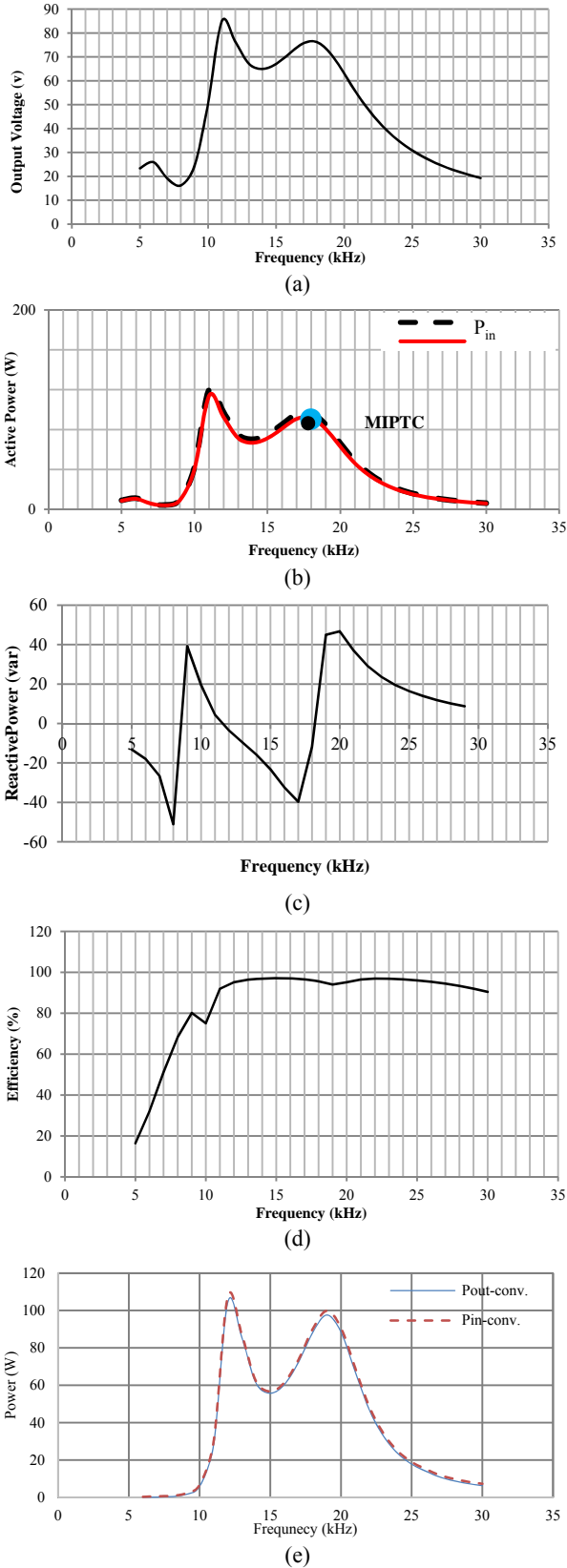
(a)

(b)

(c)

(d)

(e)

Fig. 7. Simulation results. (a) Output voltage vs. frequency, (b) input and output active powers vs. frequency, (c) input reactive power change vs. frequency, (d) IPT system efficiency vs. frequency, and (e) input and output power of primary side inverter.
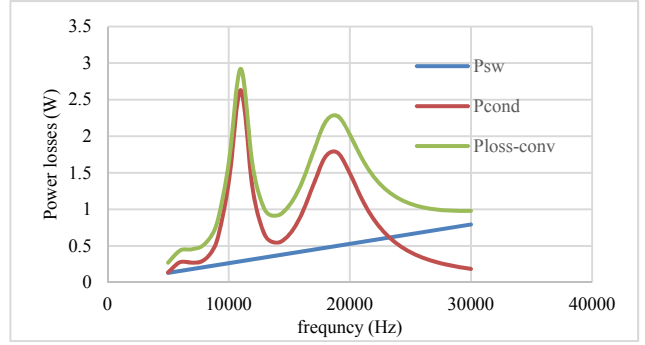

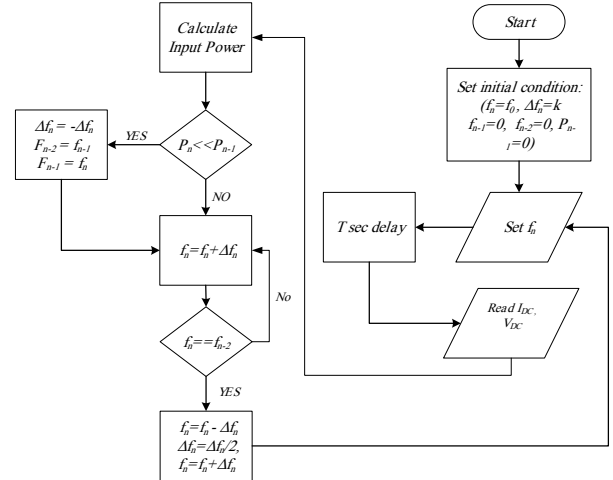Fig. 8. Power losses of the primary side inverter vs. frequency.

Fig. 9. Flowchart of the presented algorithm.

Fig. 9 shows the flowchart of the proposed algorithm. The algorithm is started by setting the initial conditions. The operation frequency of the inverter is then set as f_0. The "calculate input power" process block calculates the input power by using the IPT primary side DC current and DC voltage. If the power perturbing the IPT frequency increases, then the subsequent perturbation direction should be kept the same to reach the MIPTC; if the power decreases, then the perturbation direction should be reversed. The perturbation step size is changed adaptively to dampen the maximum power oscillations. As such, Δf_n will decrease when the algorithm reaches an operating point thrice, consecutively. As discussed in Section II, the SSR–IPT converter power transfer curve consists of two local maxima.

Given that the second peak of the power–frequency diagram is always the same as the optimal peak, the frequency tracking always begins from the right of the diagram to avoid tracking the first peak. This study assumes that the inductive power transmission converter is designed in such a way that the frequency of the maximum power of all loads is equal. However, the actual maximum power frequency of the converter is different from the designed value because of the limited changes in the primary and secondary air gaps, as well as the tolerance of resonance capacitors and the nonalignment of primary and secondary windings. Thus, the tracking begins

(a)
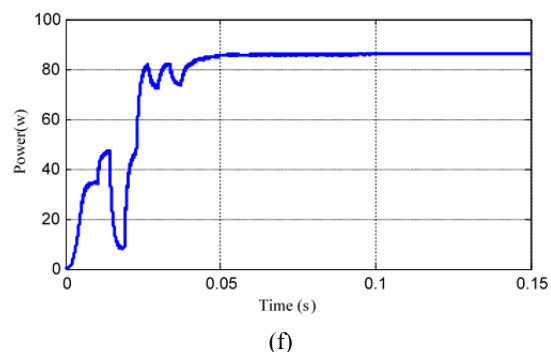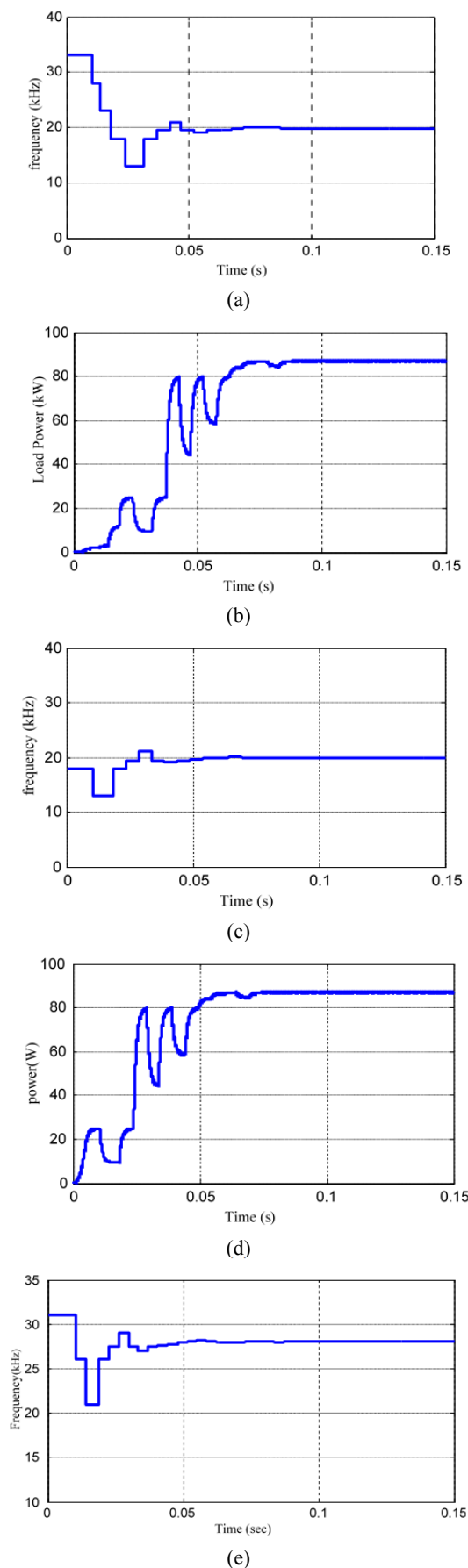

(b)

(c)

(d)

(e)

(f)

Fig. 10. (a) Frequency variation for the first test, (b) transferred power variation for the first test, (c) frequency variation for the second test, (d) transferred power variation for the second test, (e) frequency variation for the third test, and (f) transferred power variation for the third test.

by selecting a frequency that is sufficiently larger than the area of the second peak frequency.

Three tests are conducted to ensure the correct functioning of the tracking algorithm. In the first test, the starting frequency is set as 31 kHz. Fig. 10(a) shows that the tracked frequency converges to the MIPTC frequency, and the algorithm can track the MIPTCF in less than 100 ms. In the second test, the starting frequency is 19 kHz. Fig. 10(c) validates the accuracy of the algorithm. The final test demonstrates the performance of the algorithm in different MIPTC points. This test is conducted to ensure that the MIPTC frequency is achieved in other IPT conditions.

IV. EXPERIMENTAL RESULTS

The proposed tracking method was implemented on an IPT application, as shown in Fig. 12. Fig. 11 shows the block diagram of the implemented system. Table II presents the IPT system parameters. The leakage and magnetic inductances have been obtained using numerical calculations and electrical measurements.

An Advantech PC card (PCLD-7810) was used to achieve the voltage gain–frequency curve of the implemented IPT system. For each frequency change, the power, voltage, and current results are stored in a computer. Finally, the curves are constructed using the MS Excel software.

Fig. 13 shows the primary and secondary voltage waveforms at $f = 20$ kHz. In high-frequency applications, the squared wave switching pattern is used instead of the PWM. In a resonance circuit, the secondary voltage curve is sinusoidal. Figs. 14(a) and 14(b) show the output voltage and input active power waveform versus frequency. In both curves, the MIPTC value is located close to 20 kHz. The MIPTC frequency of the simulation result is approximately 18.5 kHz. This difference in value is attributed to the accuracy of the mathematical model and capacitors. Figs. 14(a) and 14(b) also show an obvious global maximum of approximately 11 kHz. As discussed previously, this extremum is unsuitable for an operation point.
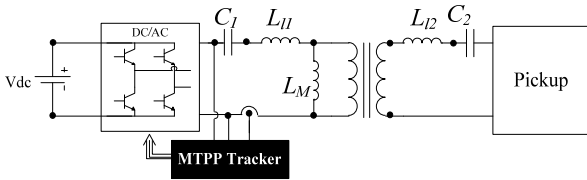
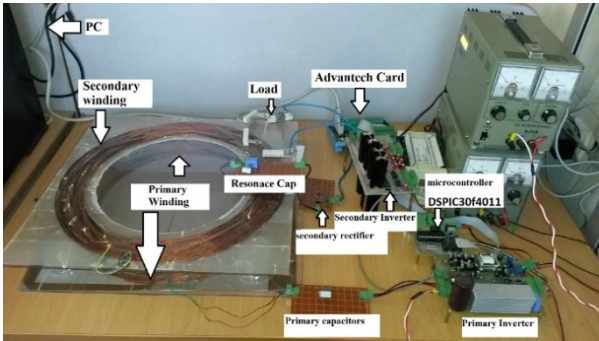Fig. 11. MIPTC-based modified IPT system model.

Fig. 12. Experimental test bench.

TABLE II
IPT Charger Parameters

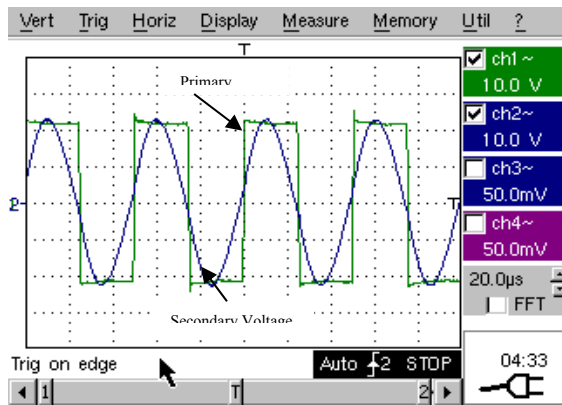| Parameter	V_{DC}	Load	L_{l1}	L_{l2}	L_M	C_1	C_2
Value	100 V	60 Ω	0.70 μH	0.70 μH	0.78 mH	0.1 μF	0.1 μF

Fig. 13. Primary and secondary voltage waveforms.

The proposed algorithm is coded in "*Visual C*" to be implemented on a control board (Advantech card) to verify the tracking method of the MIPTC. Fig. 14(c) illustrates the number of iterations required for the convergence of the frequency to the MIPTC frequency. As shown in Fig. 14(c), the tracked frequency converges to the MIPTC frequency after 10 iterations when the starting frequency of the algorithm is approximately 35 kHz. Moreover, although the starting frequency is far from the MIPTC, the algorithm can obtain an MIPTC.
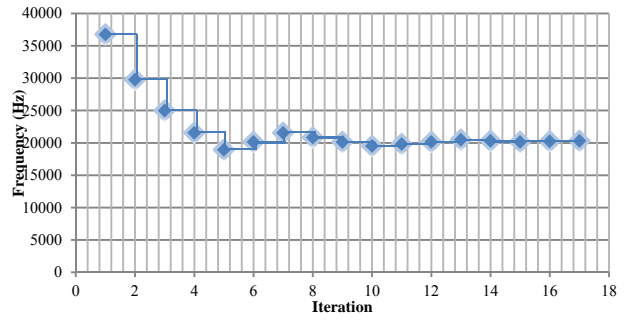
A case study is simulated to verify the performance of the proposed method in the case of any variation in alignment or distance between the pickup and the charger. The air gap of the implemented IPT is changed from 50 mm to 10 mm to
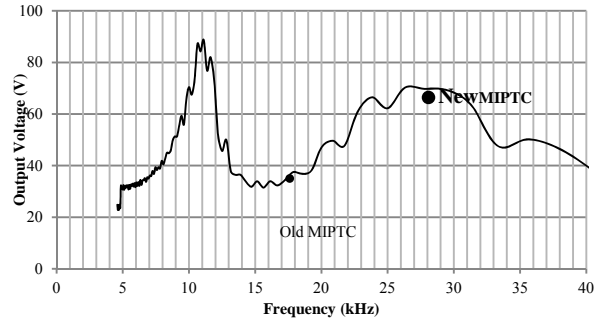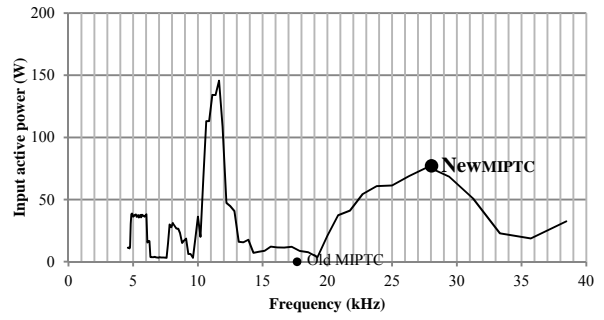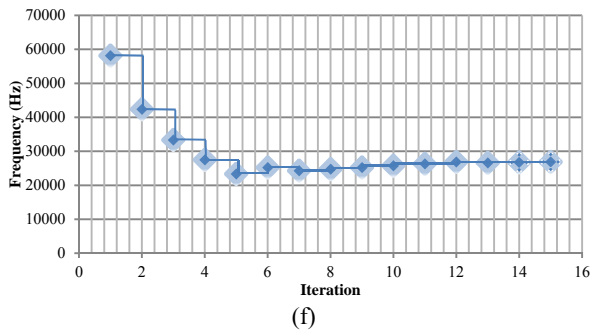

(a)

(b)

(c)

(d)

(e)

(f)
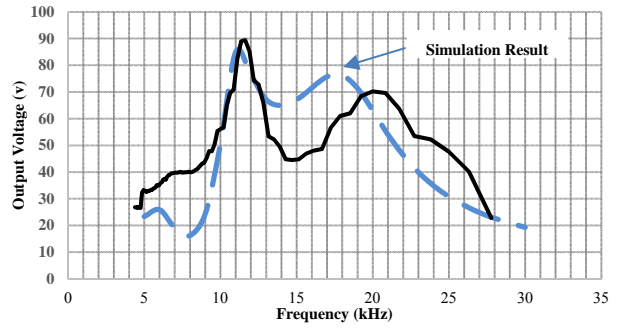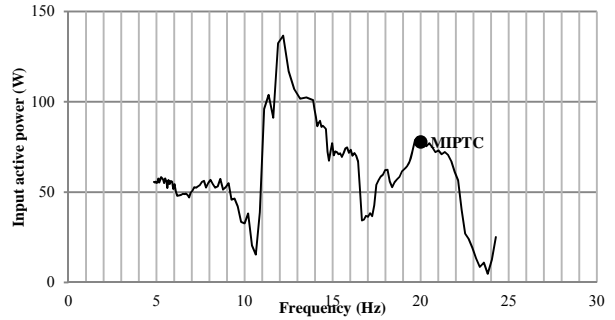
Fig. 14. (a) Output voltage for the first situation, (b) input active power for the first situation, (c) number of algorithm iterations for the first situation, (d) voltage variation for the second situation, (e) input active power for the second situation, and (f) number of algorithm iterations for second situation.

simulate this case study. Figs. 12(d) and 12(e) illustrate voltage and power as functions of frequency for the new air gap arrangement. Given the invariable resonance capacitors, any variation in IPT inductance changes the MIPTC point as shown. The comparison between Figs. 14(b) and 14(e) obviously show that, if the IPT operation frequency is the same as the old MIPTC frequency, which is 20 kHz, then the transferred power would be limited to 45 W instead of 80 W in the second test. In other words, in the absence of the MIPTC tracking algorithm, the transferred power is less than 60% of the maximum power transmission capacity. Fig. 14(f) shows that the proposed algorithm can track the new MIPTC operation frequency, which is 27 kHz in this case.

V. CONCLUSION

In IPT applications such as EV chargers, magnetic parameters change because of any variation in the alignment and position of the secondary variable relative to the primary side, which makes the optimum operation point of the IPT out of range. In this work, a novel and low-cost method, which tracks the frequency of the MIPTC, has been proposed. The determination of the MIPTC operation point for different loads and circumstances with no need for any information transfers between primary and secondary variables is the most important advantage of this method. Given the changes in the state of the charge, the load obtained by the IPTEC varies continuously with time. By simplification, a mathematical model of the IPT-based series–series and parallel–parallel resonance converters has shown that, in the SSR–IPT, an MIPTC operation point can be obtained, which is independent of the load magnitude compared with the PPR–IPT. Briefly, the IPT secondary voltage is independent of the load magnitude. The experimental results demonstrate the performance of the proposed method and validate the accuracy of the mathematical model.

REFERENCES

[1] M. Pinuela, D. C. Yates, S. Lucyszyn, and P. D. Mitcheson, "Maximizing DC-to-load efficiency for inductive power transfer," *IEEE Trans. Power Electron.*, Vol. 28, No. 5, pp. 2437-2447, May 2013.

[2] M. P. Kazmierkowski and A. J. Moradewicz, "Review of contactless energy transfer systems," *IEEE Ind. Electron. Mag.*, Vol. 6, pp. 47-55, Dec. 2012.

[3] B. Kallel, T. Keutel, and O. Kanoun, "MISO configuration efficiency in inductive power transmission for supplying wireless sensors," in *11th International Multi-Conference on Systems, Signals and Devices(SSD)*, pp. 1-5, Feb. 2014.

[4] J. Ma, Q. Yang, and H. Chen, "Transcutaneous energy and information transmission system with optimized transformer parameters for the artificial heart," *IEEE Trans. Appl. Supercond.*, Vol. 20, No. 3, pp. 798-801, Jun. 2010.

[5] P. Bauer, M. Castilla, and F. Pijl, "Control method for wireless inductive energy transfer systems with relative large air gap," *IEEE Trans. Ind. Electron.*, Vol. 60, No. 1, pp. 382-390, Jan. 2013.

[6] C. Huang, J. T. Boys, and G. A. Covic, "LCL pick-up circulating current controller for inductive power transfer systems," *IEEE Trans. Power Electron.*, Vol. 28, No. 4, pp. 2081-2093, Apr. 2013.

[7] R. Azambuja, V. J. Brusamarello, S. Haffner, and R. W. Porto, "Full four capacitor circuit compensation for inductive power transfer," in *IEEE International Instrumentation and Measurement Technology Conference (I2MTC)*, pp. 183-187, May 2013.

[8] D. J. Thrimawithana and U. K. Madawala, "A generalized steady-state model for bidirectional IPT systems," *IEEE Trans. Power Electron.*, Vol. 28, No. 10, pp. 4681-4689, Oct. 2013.

[9] M. Q. Nguyen, D. Plesa, S. Rao, and J. C. Chiao, "A multi-input and multi-output wireless energy transfer system," in *International Microwave Symposium (IMS)*, Jun. 2014.

[10] Y. C. Chuang, Y. L. Ke, H. S. Chuang, and H. K. Chen, "Implementation and analysis of an improved series-loaded resonant DC-DC converter operating above resonance for battery chargers," *IEEE Trans. Ind. Appl.*, Vol. 45, No. 3, pp. 1052-1059, May/Jun. 2009.

[11] J. Park, M. Kim, and S. Choi, "Fixed frequency series loaded resonant converter based battery charger which is insensitive to resonant component tolerances," in *7th International Power Electronics and Motion Control Conference (IPEMC)*, pp. 918-922, Jun. 2012.

[12] J. Deng, S. Li, S. Hu, C. C. Mi, and R. Ma, "Design methodology of LLC resonant converters for electric vehicle battery chargers," *IEEE Trans. Veh. Technol.*, Vol. 63, No. 4, pp. 1581-1592, May 2014.

[13] D. Murthy-Bellur, A. Bauer, W. Kerin, and M. K. Kazimierczuk, "Inverter using loosely coupled inductors for wireless power transfer," in *IEEE 55th International Midwest Symposium on Circuits and Systems (MWSCAS)*, Vol. 2, pp. 1164-1167, Aug. 2012.

[14] T. Imura, T. Uchida, and Y. Hori, "Flexibility of contactless power transfer using magnetic resonance coupling to air gap and misalignment for EV," in *International Battery, Hybrid and Fuel Cell Electric Vehicle Symposium*, Vol. 3, pp. 1-10, 2009.

[15] E. S. Kim, S. I. Kang, K. H. Yoon, and Y. H. Kim, "A contactless power supply for photovoltaic power generation system," in *Twenty-Third Annual IEEE Applied*

Power Electronics Conference and Exposition (APEC), pp. 1910-1913, Feb. 2008.

[16] U. Madawala, M. Neath, and D. J. Thrimawithana, "A power-frequency controller for bidirectional inductive power transfer systems," *IEEE Trans. Ind. Electron.*, Vol. 60, No. 1, pp. 310-317, Jan. 2013.

[17] D. A. G. Pedder, A. D. Brown, and J. A. Skinner, "A contactless electrical energy transmission system," *IEEE Trans. Ind. Electron.*, Vol. 46, No. 1, pp. 23-30, Feb. 1999.

[18] J. Lastowiecki and P. Staszewski, "Sliding transformer with long magnetic circuit for contactless electrical energy delivery to mobile receivers," *IEEE Trans. Ind. Electron.*, Vol. 53, No. 6, pp. 1943-1948, Dec. 2006.

[19] H. Sakamoto, K. Harada, S. Washimiya, K. Takehara, Y. Matsuo, and F. Nakao, "Large air-gap coupler for inductive charger," *IEEE Trans. Magn.*, Vol. 35, No. 5, pp. 3526-3528, Sep. 1999.

[20] D. Kurschner, C. Rathge, and U. Jumar, "Design methodology for high efficient inductive power transfer systems with high coil positioning flexibility," *IEEE Trans. Ind. Electron.*, Vol. 60, No. 1, pp. 372-381, Jan. 2013.

[21] S. Hasanzadeh, S. Vaez-Zadeh, and A. H. Isfahani, "Optimization of a contactless power transfer system for electric vehicles," *IEEE Trans. Veh. Technol.*, Vol. 61, No. 8, pp. 3566-3573, Oct. 2012.

[22] U.-M. Jow and M. Ghovanloo, "Design and optimization of printed spiral coils for efficient transcutaneous inductive power transmission," *IEEE Trans. Biomed. Circuits Syst.*, Vol. 1, No. 3, pp. 193-202, Sep. 2007.

[23] V. J. Brusamarello, Y. B. Blauth, R. Azambuja, I. Muller, and F. R. de Sousa, "Power transfer with an inductive link and wireless tuning," *IEEE Trans. Instrum. Meas.*, Vol. 62, No. 5, pp. 924-931, May 2013.

[24] A. P. Sample, S. Member, D. T. Meyer, and J. R. Smith, "Analysis, experimental results, and range adaptation of magnetically coupled resonators for wireless power transfer," *IEEE Trans. Ind. Electron.*, Vol. 58, No. 2, pp. 544-554, Feb. 2011.

[25] E. Waffenschmidt and T. Staring, "Limitation of inductive power transfer for consumer applications," in *13th European Conference on Power Electronics and Applications (EPE)*, pp. 1-10, Sep. 2009.

[26] H. H. Wu, A. Gilchrist, K. Sealy, P. Israelsen, and J. Muhs, "A review on inductive charging for electric vehicles," in *IEEE International Electric Machines & Drives Conference (IEMDC)*, pp. 143-147, May 2011.

[27] M. L. G. Kissin, J. T. Boys, and G. A. Covic, "Interphase mutual inductance in polyphase inductive power transfer systems," *IEEE Trans. Ind. Electron.*, Vol. 56, No. 7, pp. 2393-2400, Jul. 2009.

[28] J. L. Villa, J. Sanz, J. F. S. Osorio, and A. Llombart, "High-misalignment tolerant compensation topology for ICPT systems," *IEEE Trans. Ind. Electron.*, Vol. 59, No. 2, pp. 945-951, Feb. 2012.

[29] W. G. Hurley and M. C. Duffy, "Calculation of self-and mutual impedances in planar sandwich inductors," *IEEE Trans. Magn.*, Vol. 33, No. 3, pp. 2282-2290, May 1997.

[30] T. Esram and P. L. Chapman, "Comparison of photovoltaic array maximum power point tracking techniques," *IEEE Trans. Energy Convers.*, Vol. 22, No. 2, pp. 439-449, Jun. 2007.

Mohammad Hassan Ameri received his B.S. degree in Electrical Engineering from Shahroud University of Technology in 2007 and his M.S. degree in Power Electronics Engineering from Tehran University in 2010. He is currently working toward his Ph.D. in the Electrical and Computer Engineering Department at Tarbiat Modares University, Tehran, Iran. His research interests are in the areas of power electronic systems, contactless power transfer, and renewable energy systems.

Ali Yazdian Varjani received his B.S. degree from Sharif University of Technology in 1989 and his M.Eng. and Ph.D. degrees in Electrical Engineering from the University of Wollongong, Australia in 1995 and 1999, respectively. Since 1999, he has been with Tarbiat Modares University, Tehran, Iran as an Assistant Professor in the Department of Electrical and Computer Engineering. His major research activities are in the areas of digital signal processing applicable to harmonics (power quality) and power electronics based on drive systems. His current academic interests include a variety of research issues associated with "information and communication technology," including Internet-enabled services, ad hoc networking, and network security and control.

Mustafa Mohamadian (M'04) received his Ph.D. degree in Electrical Engineering, specializing in Power Electronics from the University of Calgary, Alberta, Canada in 1997. Currently, he is an Associate Professor at Tarbiat Modares University, Tehran, Iran. Dr. Mohamadian's main research interests include analysis, modeling and control of power converters, renewable energy systems, Uninterruptible Power Supplies and motor drives.